Ferroelectric Polarization-Induced Performance Enhancements in $BiFeO_3$-Based Photoanodes for Photoelectrochemical Water Splitting

Michael Gunawan[1], Owen Bowdler[2], Shujie Zhou[1], Xueqing Fang[2], Qi Zhang[2,3], Yasuhiro Sakamoto[2], Kaiwen Sun[4], Denny Gunawan[1], Shery L.Y. Chang[2,5], Rose Amal[1], Nagarajan Valanoor[2], Judy N. Hart[2]*, Jason Scott[1], and Cui Ying Toe[1,6]*

1 Particles and Catalysis Research Group, School of Chemical Engineering, UNSW Sydney, NSW, 2052, Australia

2 School of Materials Science and Engineering, UNSW Sydney, NSW 2052, Australia

3 CSIRO, Manufacturing, Lindfield, NSW 2070, Australia

4 School of Photovoltaic and Renewable Energy Engineering, UNSW Sydney, NSW 2052, Australia

5 Electron Microscope Unit, Mark Wainwright Analytical Centre, UNSW Sydney, NSW 2052, Australia

6 School of Engineering, The University of Newcastle, Callaghan, NSW 2308, Australia

Corresponding authors: j.hart@unsw.edu.au; cuiying.toe@newcastle.edu.au

Keywords: Bismuth ferrite, Bismuth vanadate, Ferroelectric photoanode, Photoelectrochemical, Water splitting.

Abstract

Photoelectrochemical (PEC) processes will play a crucial role in future clean energy systems, however severe charge recombination and sluggish charge transfer kinetics have hindered their practical adoption. Exploiting ferroelectric polarization-controlled charge dynamics promises an additional lever that can potentially enable the performance limits of traditional static photoelectrodes to be surpassed. Here we report one of the most notable ferroelectric polarization-induced photocurrent enhancements, using a heterostructure of the multiferroic bismuth ferrite (BFO) and the photoactive bismuth vanadate (BVO) in a neutral pH electrolyte. In contrast to previous works, we report enhancements for both poling directions, of 136% for down-poled BFO/BVO and of 70% for the up-poled BFO/BVO, at 1.23 V_{RHE} in comparison to the unpoled, delivering a Faradaic efficiency of more than 95% for prolonged oxygen evolution reaction. Extensive PEC and surface analyses complemented by DFT calculations reveal the improvements are attributed to the modulation of gradients in BFO band energies, changes in band-bending and offsets at the interfaces. Given the scalability of the employed sol-gel synthesis

https://doi.org/10.26434/chemrxiv-2024-lh925-v2 **ORCID:** https://orcid.org/0009-0001-7364-4574

method and the use of environmentally benign materials and PEC conditions, our findings pave the way for multifunctional materials as new-generation agile and dynamic catalyst and photoelectrode systems.

Introduction

To mitigate the effects of climate change, a transition to renewable and clean energy sources is crucial to sustainably meet the escalating global demand for energy.[1] Harnessing solar energy to drive photoelectrochemical (PEC) reactions is promising for the sustainable production of energy carriers and chemical fuels, including hydrogen by water splitting.[2-5] PEC water splitting efficiency remains low due predominantly to severe bulk charge recombination and the sluggish oxygen evolution reaction (OER) at the photoanode surface.[6] An approach to overcome the constraints is to employ ferroelectric-based photoanodes. Their permanent and reversible spontaneous electric polarization can facilitate photo-induced charge separation and suppress charge recombination.[7-9] Further, polarization offers two distinct chemical surfaces of the material which can endow the photoanode with selective adsorption and desorption abilities and provide an alternate route to engineer reaction rates.[10] These intrinsic abilities, namely charge recombination suppression via an internal field and switchable surface chemistry, have invoked tremendous interest in innovative ferroelectric-based photoelectrode engineering.[11,12].

Early efforts to apply ferroelectric materials as photoanodes predominantly examined barium titanate ($BaTiO_3$). [13-16] Augurio *et al*. demonstrated enhanced PEC performance of a poled $BaTiO_3$ photoanode compared to the virgin unpoled state.[13] However, the reported $BaTiO_3$ has a band gap of 3.3 eV, restricting solar light absorption to less than 5% of solar photons. To better harness the solar spectrum while providing enough energy to drive the water splitting reaction efficiently, a material with a band gap below 2.7 eV is required.[6,17]

Recently the iconic single-phase multiferroic bismuth ferrite ($BiFeO_3$, BFO) has attracted attention as a promising visible-light photoelectrocatalyst due to its non-toxic nature, 2.2 – 2.7 eV band gap, unique domain-wall properties and robust room temperature multiferroic properties.[18-21] Li and co-workers reported a 110% enhancement in photocurrent density of down-polarized BFO due to improved charge separation and transport.[22] However, recombination losses remain persistently high and PEC performances have been poor. Typical photocurrent densities for PEC water splitting lie in the range of tens of microampere which is not sufficient for practical device implementation.[23,24] In the case of BFO thin films (or any oxide ferroelectric thin film), the most impressive performance is often realized for epitaxial films fabricated on specialized oxide substrates using sophisticated capital-intensive heteroepitaxy techniques. This raises the issue of practical viability regarding costs and sample scalability.

An alternative to ferroelectrics as stand-alone photoelectrodes is to incorporate them with state-of-the-art photoactivate materials like bismuth vanadate ($BiVO_4$, BVO). This can potentially give significantly enhanced performance while exploiting the ferroelectric polarization to overcome inherent BVO limitations comprising poor charge separation and high recombination losses.[25-27] Xie *et al.* used a BFO/BVO heterojunction to enhance photocurrent density (0.28 $mA.cm^{-2}$ at 1.23 V_{RHE}) compared to stand-alone BFO and BVO layers.[25] Manipulating the ferroelectric polarization state amplified the effect, with the photocurrent density further improved (0.32 $mA\ cm^{-2}$) when the BFO/BVO was up-poled.

Whilst boosting the photocurrent densities via electric-field induced poling of ferroelectrics has been observed, to-date any enhancement happens only when poling in one direction. Poling in the opposite direction decreases photocurrent, curtailing the use of ferroelectric composites. Restricting the enhancement to one polarization direction does not allow realization of the full material potential. Accessing the two polarization states to dynamically create distinct chemical surfaces would enable regulated adsorption and desorption at the photoanode surface while simultaneously maintaining strong photocurrent generation – a particular capability unique to ferroelectric surfaces, which in principle can help overcome the Sabatier principle.[11] From a fundamental perspective, direct evidence of ferroelectric switching on the electronic properties and surface chemical states of a BFO/BVO photoanode remains elusive. Other reports typically provide photocurrent performance without detailed physico-chemical characterization of the poled states.[25,28] Additionally, computational models that can accurately capture the subtle roles played by various physico-chemical factors *in-operando* are lacking. Demonstrating an environmentally sustainable ferroelectric polarization enhanced photoelectrode with complete fundamental behavioral understanding continues to elude the research community.

The current work exploits the correlations between polarization switching, band energy shifts, band energy gradient modulations, and changes in the water/BFO interaction to overcome the challenges inherent within a BFO/BVO photoanode and demonstrate significant polarization-induced PEC performance (**Fig. 1a**). A comprehensive suite of PEC and surface characterization methods complemented by rigorous density functional theory (DFT) calculations are engaged to systematically unravel the individual effects of the various factors that affect PEC performance. Whilst integrating BFO with BVO is shown to improve visible-light absorption and charge separation capabilities, yielding a more than 4-fold enhancement in photocurrent density compared to bare BFO on a fluorine-doped tin oxide (FTO) substrate at 1.23 V_{RHE},[25,29] what is striking is that our report demonstrates enhanced PEC performance for both polarization ("up" and "down") directions, an effect hitherto unseen for any ferroelectric-based photoelectrochemical study. Characterization indicates the unique behavior derives from competition between band shifting, band energy gradient modulation, and surficial BFO/water interaction. When the BFO layer is down-poled, the BFO/BVO performance improves by 136%, offering one of the highest reported photocurrent improvements due to ferroelectric polarization switching. Further, a 70% enhancement of photocurrent density arises when the BFO layer is up-poled. Prolonged illumination shows that the BFO/BVO photoanodes are stable for water splitting reactions with a Faradaic efficiency greater than 95% in all cases.

Crucially, the BFO/BVO heterojunction system is fabricated by a chemical solution deposition (CSD) method on FTO, with the PEC measurements conducted in an aqueous neutral pH electrolyte. This signifies distinct scaling capability and the capacity for practical large-array ferroelectric-based PEC systems. The study upgrades ferroelectric-based photoelectrodes with tunable electronic structures and surface chemistry to control surface adsorption/desorption, advancing beyond the fundamental limitations of traditional photoelectrodes to reach otherwise unattainable efficiencies towards desired products.

Results and discussion

A BVO nanocrystalline layer was deposited on a commercially available FTO substrate and heat treated in air at 500 °C for 60 mins, followed by deposition of BFO layer. The bilayer was heated in air at 450 °C for 60 mins. The BFO layer thickness is critical for good light utilization by the BFO/BVO and facilitating ferroelectric polarization without substrate pinning by the BVO. A 20 nm BFO layer delivered optimal PEC activity under visible-light irradiation (**Supplementary Fig. S1**), and therefore used for all subsequent measurements. Scanning electron microscopy (SEM) (**Supplementary Fig. S2a**) of the bare BVO sample reveals a porous, uniform nanoparticle coating on the FTO. The particle size is larger following BFO deposition (**Supplementary Fig. S2b**), indicating a BFO layer coated on the BVO. The annular dark field transmission electron microscopy (ADF-TEM) image of the BFO/BVO shows the 20 nm BFO layer on the 100 nm BVO film (**Supplementary Fig. S3**).

The X-ray diffraction (XRD) pattern of bare BVO (**Supplementary Fig. S4**) displays peaks representing monoclinic BVO (ICSD:100603). BFO deposition does not alter the XRD pattern, attributable to the low BFO loading. The BFO presence is evident for BFO/BVO with a thicker BFO layer (**Supplementary Fig. S4**). The peak at 27° represents the BFO (012) plane (ICSD: 196250). Selected area electron diffraction (SA-ED) patterns of the BFO/BVO (**Supplementary Fig. S5a-b**) reveal polycrystalline BFO with [100] and [010] growth directions of R3c hexagonal BFO on BVO crystals. X-ray absorption spectroscopy (XAS) confirms the BFO presence (**Supplementary Fig S6**) as well as the Fe^{3+} oxidation state in BFO/BVO.

The piezoelectric response phase and amplitude signals were measured under an applied DC bias, with phase switching instigating the ferroelectric effect. The BVO thin film did not offer a response (**Supplementary Fig. S7a**) on exposure to ±9V DC bias, illustrating the non-ferroelectric nature of BVO. In contrast, phase switching and butterfly loops were observed for the bare BFO (**Supplementary Fig. S7b**) and BFO/BVO **(Supplementary Fig. S8a)** films, demonstrating their strong ferroelectricity.[15] The BFO/BVO thin film, which is dominated by downward polarization, displayed a phase signal with a nearly 180° domain switching phenomenon, accompanied by robust domain walls, upon reversal of the DC bias **(Supplementary Fig. S8b**).

The BFO/BVO thin film was employed as a photoanode for PEC water splitting. Compared to the individual components, the BFO/BVO photoanode delivers a better PEC performance. Linear sweep voltammetry (LSV) (**Fig. 1b**) and light-on/light-off chronoamperometry (**Fig. 1c**) reveal the BFO layer on BVO increased the photocurrent density to 0.25 mA cm^{-2} at 1.23 V_{RHE}, surpassing the photocurrent densities of bare BVO and BFO by greater than 6-fold and 10-fold, respectively **(Supplementary Fig. S1)**. The enhancements are attributed to: (i) a better light absorption ability (UV-Vis spectra, **Supplementary Fig. S9**); and (ii) improved charge transfer associated with the BVO:BFO heterojunction (**Supplementary Fig. S10**).[30] Heterojunction formation can induce an internal electric field at the BVO:BFO type-II interface. Charge separation is accelerated by driving photogenerated electrons from the BFO conduction band (CB) to the BVO CB, while holes move from the BVO valence band (VB) to the BFO VB.[25] The augmented charge separation is confirmed by photoelectrochemical impedance spectroscopy (PEIS) (**Supplementary Fig. S11)**. The equivalent circuit and parameters are given in **Supplementary Fig. S11** and **Supplementary Table S2**, respectively. The bulk charge transfer resistance (R_{ct}) of BVO decreases from 11500 Ω to 484 Ω following BFO deposition, confirming the accelerated charge separation induced by the heterojunction. The impedance at the semiconductor-electrolyte interface (R_f) was slightly lower.

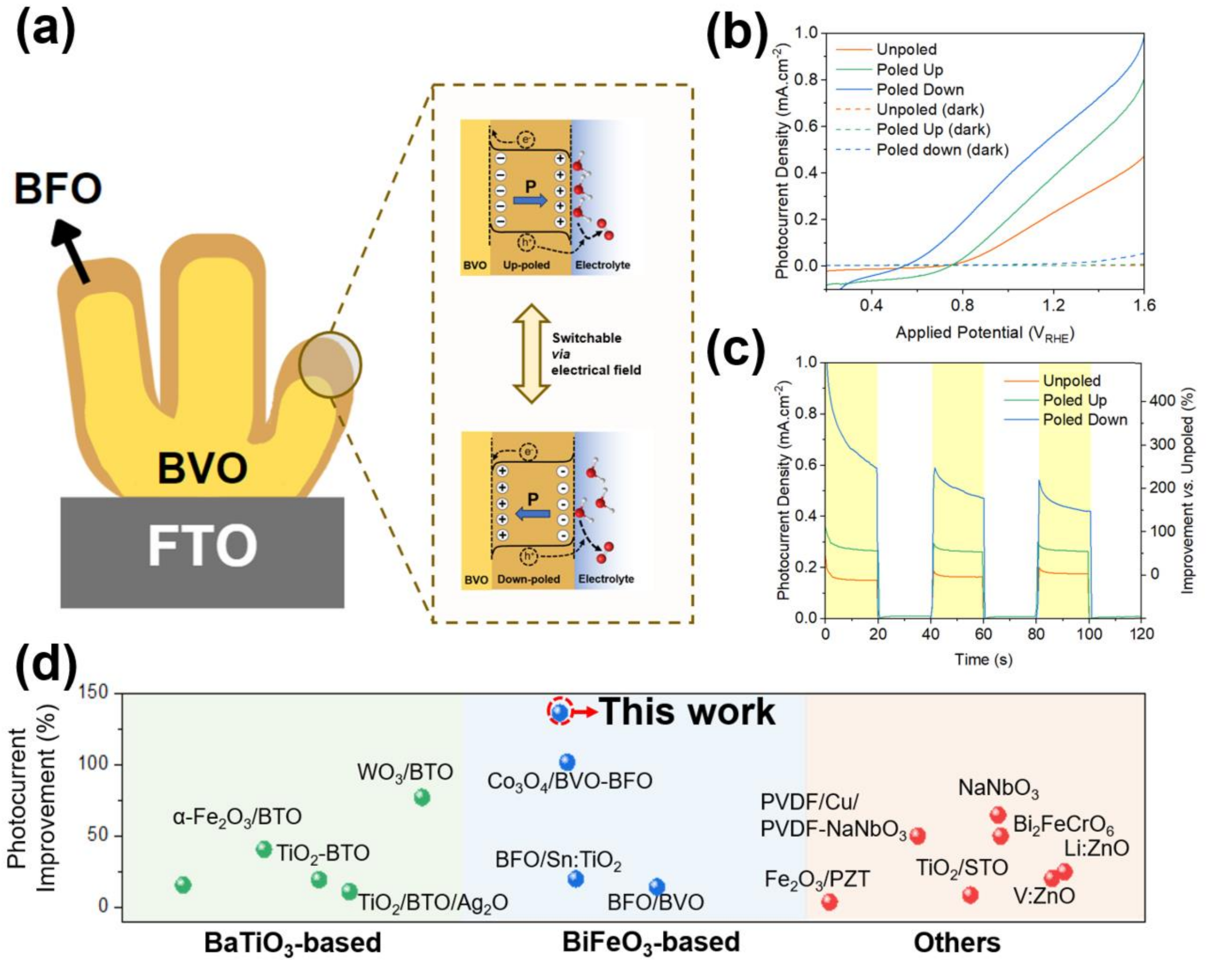

Figure 1. (a) Schematic depicting BFO/BVO structure with polarization-driven switchable surface state and electronic structure of BFO. **(b)** Linear sweep voltammetry profiles and **(c)** light-on and light-off chronoamperometry curve response at 1.1 V_{RHE} of the BFO/BVO photoanode measured in 0.1 M phosphate buffer solution under AM 1.5 G, 100 mW cm^{-2} illumination. **(d)** Comparison of the photocurrent density improvement at 1.23 V_{RHE} for PEC water splitting for the BFO/BVO photoanode after downward poling in this work with other ferroelectric-based photoanodes; full data are listed in **Supplementary Table S1**.

Electrochemical poling was used to pole the BFO/BVO by ±8 V in 0.1 M lithium perchlorate electrolyte in propylene carbonate (**Supplementary Fig. S12**). Downward polarization boosted the photocurrent density by 136% (0.59 mA cm^{-2} at 1.23 V_{RHE}) compared to unpoled BFO/BVO, accompanied by a negative 175 mV shift in the on-set potential (**Fig. 1b**). Upward polarization increased the photocurrent density by 70% (0.42 mA cm^{-2} at 1.23 V_{RHE}) compared to unpoled BFO/BVO with an accompanying 30 mV positive shift in the on-set potential. The downward polarization improvement represents a distinct advance in photocurrent enhancement for ferroelectric-based composite photoanodes compared to available literature (**Fig. 1d**, **Supplementary Table S1)**. Note that the current BFO/BVO system was not doped or loaded with a cocatalyst. Further, PEC measurements were conducted in a neutral 0.1 M phosphate buffer solution compared to other studies which employed alkaline electrolytes.[28,31-37] Unpoled and polarized BFO/BVO photoanode stability was verified by 2.5h of continuous water splitting (**Supplementary Fig. S13**, **Supplementary Fig. S14**). A Faradaic efficiency greater than 95% was observed for the unpoled and poled samples indicating efficient charge consumption for the water splitting reaction.

The bulk charge separation efficiency (η_{bulk}) and charge injection efficiency (η_{inj}) for BFO/BVO in the different polarization states were determined from LSV curves for the sulfite oxidation reaction (**Supplementary Fig. S15**, **Supplementary Fig. S16**). The unpoled BFO/BVO exhibited η_{bulk} and η_{inj} values of 8.7% and 27.3% at 1.23 V_{RHE}, respectively. The up-poled BFO/BVO η_{bulk} and η_{inj} values are 11.7% and 17.3%, respectively, suggesting improved charge transfer within the photoanode bulk with a higher recombination rate at the SEI for up-poled compared with unpoled BFO/BVO. Conversely, η_{bulk} and η_{inj} for down-poled BFO/BVO are higher (16.4% and 33.6%, respectively) than the unpoled BFO/BVO, indicating improved charge transfer within the bulk photoanode and at the SEI.

Our results are in stark contrast to the previous work on a similar BFO/BVO system by Xie *et al*.[25] They reported a (much smaller) increase in PEC performance with up-poling (20% *vs*. 70% here), but critically found a severely decreased current, by ~75%, for down-poling, compared to the 136% enhancement in photocurrent for down-poling reported here. Whilst pinpointing the exact origins for these different behaviors is not possible due to challenges associated with provenance of samples and details of PEC measurement, we believe one key difference is the method of poling. The XPS and DFT results show that the BFO surface termination is strongly influenced by the interaction between the polarized surface and water. We believe that poling by electrochemical method (in our work) *vs*. in air (done by Xie *et al.*) will give different surface terminations and hence different PEC performance and can explain differences between our results and previous.[25] An improved PEC performance driven by electrochemical poling was indeed recently found for ultrathin epitaxial BTO films[10] and by Yang *et al.* who found that down-poling BVO/BFO in aqueous solution gave better performance than up-poling.[28]

PEIS analysis of BFO/BVO in different polarization states supports the charge separation trends (**Fig. 2a**, **Supplementary Table S2**). The R_f value of up-poled BFO/BVO is higher compared to unpoled BFO/BVO (**Fig. 2b**), confirming the sluggish charge transfer at the SEI. The lower up-poled R_{ct} value reflects the enhanced bulk charge separation efficiency within the up-poled BFO/BVO. The R_{ct} and R_f values are significantly lower for down-poled than unpoled BFO/BVO, consistent with the charge separation efficiency values. This confirms the enhanced charge transfer both within and at the SEI for down-poled BFO/BVO. The cumulative effects of R_s, R_f and R_{ct} (**Fig. 2b**) are consistent with the up-poled sample imparting moderately improved performance compared with unpoled and down-poled samples imparting significantly improved performance.

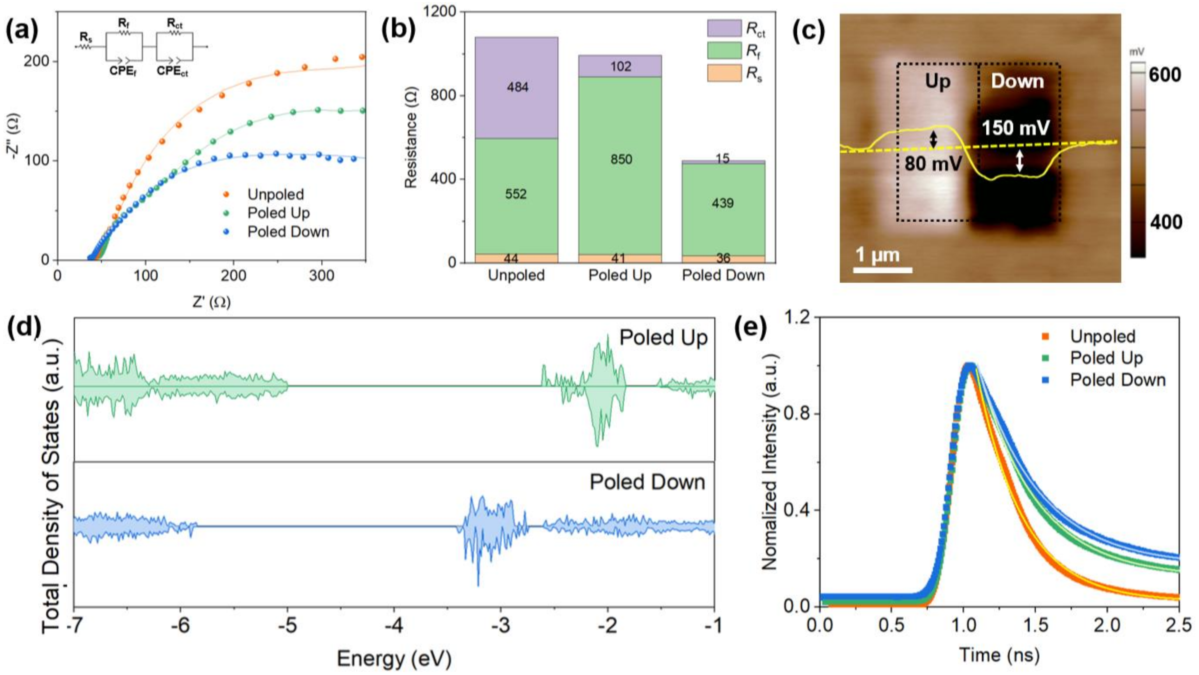

Figure 2. (a) Nyquist plots from photoelectrochemical impedance spectroscopy (PEIS) of BFO/BVO at 1.1 V_{RHE}; inset in (a) shows the equivalent circuit employed to calculate the parameters in **Supplementary Table S2** and **(b)** comparison of these values for the different polarization states. **(c)** KPFM and surface potential line profile of the BFO/BVO photoanode. **(d)** Calculated DFT total

densities of states (DOS) of up-poled and down-poled BFO. **(e)** TRPL curves of the BFO/BVO photoanode with different polarization states (the excitation wavelength is 470 nm). The fitted lines are shown in yellow.

The variations in η_{inj} and R_{f} for the two polarization states are attributable to differences in band bending at the SEI, which are governed by changes in the BFO Fermi level and the electrolyte oxidation potential difference.[38] Kelvin probe force microscopy (KPFM) of the BFO/BVO shows that polarization modifies the contact potential difference (CPD, **Fig. 2c**). Down-poled BFO/BVO exhibits a 150 mV decrease in CPD relative to the unpoled case, representing a Fermi level shift to lower energy and enhanced band bending at the SEI (**Fig. 3b**).[39] The finding agrees with a report by Li *et al.*[22] A converse effect was observed for up-poled BFO/BVO where the Fermi level shifted (by 80 mV) to a higher energy, reflecting a smaller degree of band bending and slower charge transfer kinetics at the SEI (**Fig. 3c**). The η_{inj} and R_{f} values of unpoled BFO are closer to down-poled than up-poled BFO although the CPD value is closer to up-poled BFO. The unpoled sample comprises both up-poled and down-poled domains, with the CPD value reflecting the average of the two. The down-poled regions, with more favorable band alignment at the SEI, are likely to be the dominant reaction sites, with the η_{inj} and R_{f} values being more similar to down-poled BFO.

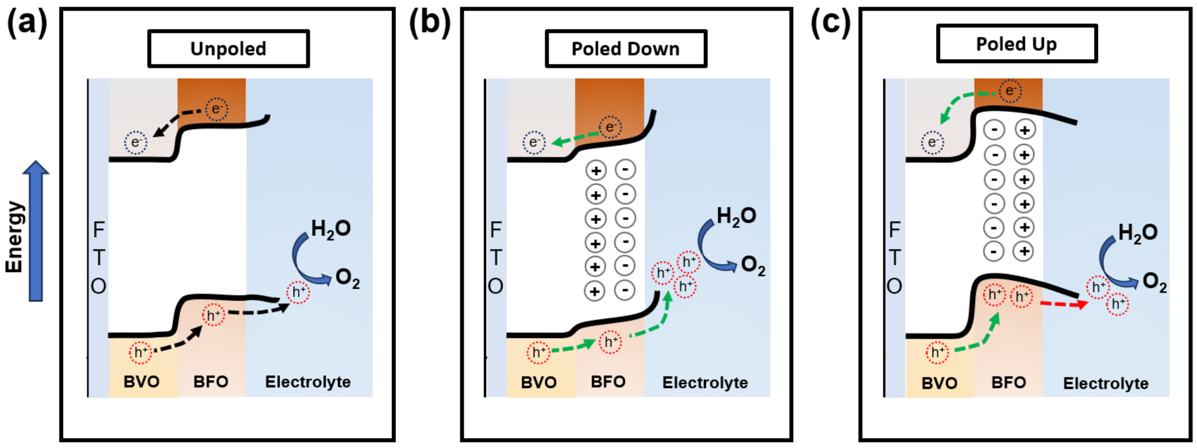

Figure 3. Schematic of the band positions in (a) unpoled, (b) down-poled and (c) up-poled BFO/BVO, illustrating the effects on charge transport of electronic band shifting and gradients in band energies within the BFO layer due to poling. The color of arrows indicating the relative rates of charge transfer, with faster (green) and slower (red) compared to the unpoled as benchmarks (black).

Valence band X-ray photoelectron spectroscopy (VB XPS, **Supplementary Fig. S17**) showed a BFO VB shift (0.23 eV) to a lower energy following downward polarization and a higher energy shift (0.21 eV) with upward polarization. The density of states (DOS) calculated by DFT (**Fig. 2d**) indicates a shift (~0.9 eV) to lower energies by the CB and VB when transitioning from up-poled to down-poled. Combined, the findings suggest the change in band energies and accompanying degree of band bending at the SEI are the source of the changes in η_{inj} and R_{f} with polarization.

Time-resolved photoluminescence (TRPL) spectroscopy (**Fig. 2e**, **Supplementary Table S3**) show the unpoled BFO/BVO photoanode possesses the shortest carrier lifetime (0.71 ns). The up-poled and down-poled BFO/BVO photoanodes exhibit longer carrier lifetimes (0.92 ns and 1.01 ns, respectively). The order of lifetimes across the samples is consistent with both the order of η_{bulk} and R_{ct} values and the photocurrent magnitudes, validating the bulk charge transfer improvements in BFO/BVO induced by ferroelectric polarization and the influence on PEC performance.

Relative to the unpoled BFO/BVO (**Fig. 3a**), the increase in η_{bulk} and decrease in R_{ct} for the down-poled sample are attributed to two factors (**Fig. 3b**): (i) the electric field across the BFO layer arising from polarization will induce a gradient in the band energies, promoting hole transport to the SEI (indicated by increased η_{inj} and decreased R_{f}) and electron transport to the BVO layer;[25,40] (ii) the negatively shifted electronic states in the down-poled BVO/BFO reduce the band offsets at the heterointerface, reducing the photogenerated charge transfer energy barrier across the BFO/BVO interface,[41] invoking more efficient charge transfer in down-poled BFO/BVO. Conversely, the reduced band offsets diminish the charge transfer driving force across the interface and the extent of BVO layer band bending near the interface, exposing a tradeoff between band shifting and BFO gradient modulation phenomena in poled BFO/BVO.

The tradeoff is reversed for up-poled BFO/BVO (**Fig. 3c**). The larger band offset at the heterointerface facilitates band bending and charge separation at the BFO/BVO interface corresponding to the increased η_{bulk} value (the effect may be reduced by the increased energy barrier for charge separation due to the larger offset [25,40]). The gradient in the bands in the up-poled BFO layer will impair hole transport to the SEI, supported by the decreased η_{inj} and increased R_{f}. The tradeoff between opposing polarization-induced effects on band energies has been noted in a study by Yang *et al.*,[40] on a ferroelectric-based $BaTiO_3/TiO_2$ heterostructure photoanode. They found the effect of band gradients in the ferroelectric layer was more dominant in with a thick (40 nm) BTO layer, while changes in band bending at the heterointerface were more significant with a thin (5 nm) BTO layer. The change in the dominant effect flipped the best performance between down-poled (gradient effect dominates) and up-poled (interface band bending dominates). In our work, the effect of the band gradients in BFO appears to dominate over the interface band bending effect, resulting in the η_{bulk} being higher, R_{f} being lower and PEC performance being better for the down-poled than the up-poled sample. However, the presence of at least one of these effects, in combination with the effects of coherent domain structure, results in both poled samples having higher η_{bulk}, lower R_{f}, and better PEC performance than the unpoled sample. The balance between the competing factors may explain differences in the effects of polarization on PEC performance observed here and in previous work, with the balance, and hence which polarization state gives best performance, being affected by, for example, the thickness of the ferroelectric layer and the poling conditions such as voltage and time (**Supplementary Table S1**). Up and down poling may also increase η_{bulk} due to a more coherent domain structure with fewer domain walls, reducing barriers to charge transport.[42]

The Fe 2p X-ray Photoelectron Spectroscopy (XPS) spectra illustrates a decrease in the Fe^{2+}:Fe^{3+} ratio for the up-poled sample compared with unpoled and down-poled (**Supplementary Fig. S19**), consistent with the ferroelectric polarization increasing the positive charge at the surface. The Fe^{2+}:Fe^{3+} ratio is similar between the unpoled and down-poled samples, confirming that the unpoled sample is predominantly down-poled. Note that, while the iron oxidation state at the BFO surface was found by XPS to be Fe^{2+} dominant, XAS (**Supplementary Fig. S6**) confirmed that the bulk BFO has an oxidation state of Fe^{3+}, verifying the changes are happening predominantly at the surface and the bulk material is BFO.

The O 1s XPS spectra (**Fig. 4a**) of unpoled BFO/BVO can be deconvoluted into three peaks at 531.1 eV, 530.6 eV and 529.5 eV, attributable to physisorbed water at the BFO surface (O_{W-P}), lattice hydroxide (i.e. protons adsorbed on surface lattice oxygen, O_{L-H}) and lattice oxygen (O_L), respectively.[43] A subtle peak at 533.2 eV represents chemisorbed water molecules (O_{W-C}) at the BFO surface.

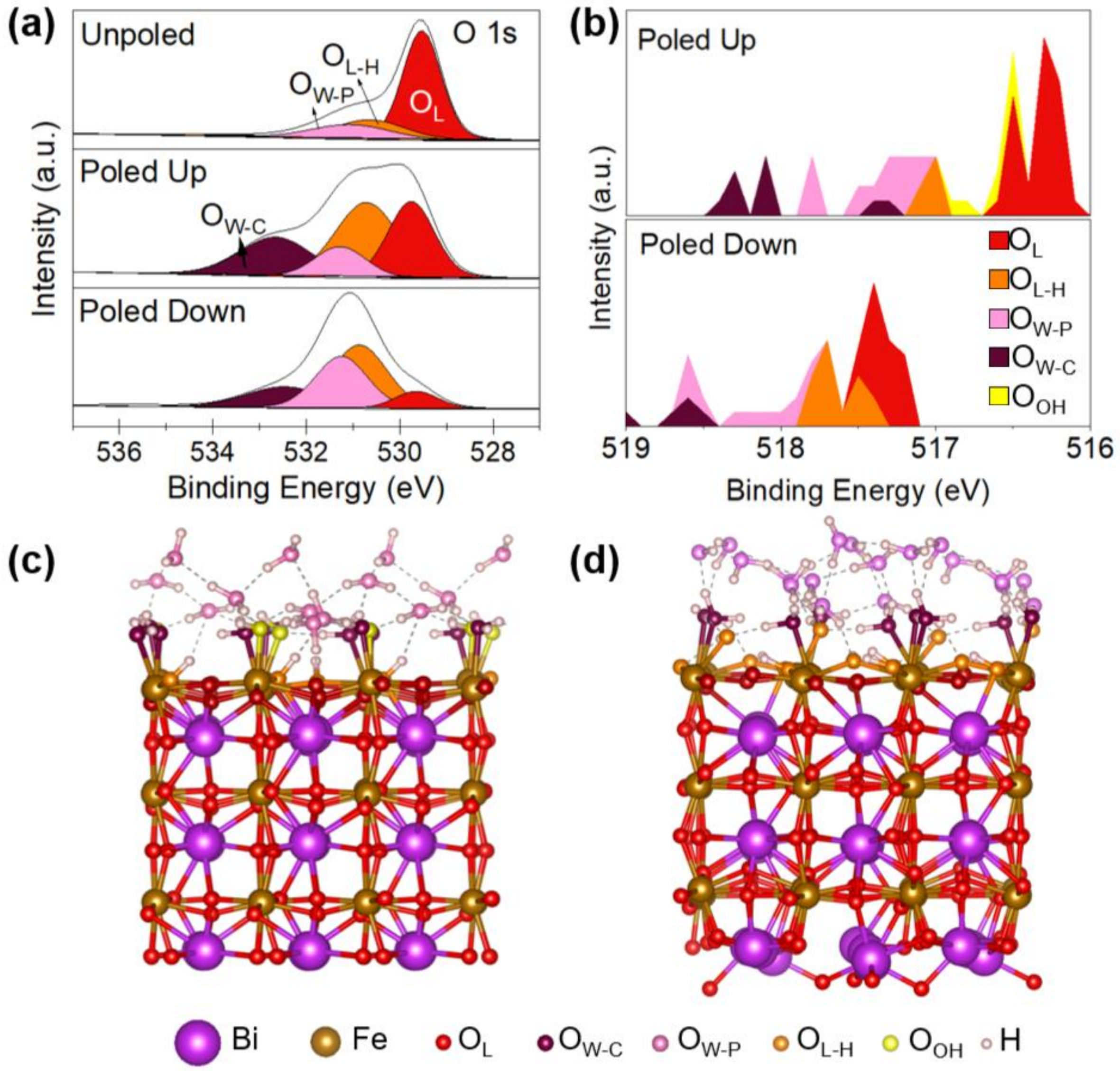

Figure 4. (a) O 1s XPS spectra of the BVO/BFO photoanodes. **(b)** Simulated XPS spectra of BFO obtained from the optimized DFT models of **(c)** up-poled and **(d)** down-poled BFO showing various oxygen-containing species at the surface.

The up-poled BFO/BVO exhibits a decreased O_L peak intensity, while the $O_{L\text{-}H}$, $O_{W\text{-}C}$ and $O_{W\text{-}P}$ peaks are increased compared to the unpoled sample (**Fig. 4a**). DFT calculations indicate the up-poled surface can spontaneously dissociate water molecules, converting some surface lattice O to OH (**Fig. 4b-c**) in agreement with previous work.[44] When the up-poled BFO/BVO sample is exposed to water (e.g., during poling) dissociation of the water molecules promotes the $O_{L\text{-}H}$ peak (530.7 eV). Further, oxygen vacancies in the BFO bulk can migrate toward the surface under upward polarization.[45,46] Surface oxygen vacancies on the up-poled BFO/BVO will be filled by OH from dissociated water, contributing to the increased $O_{L\text{-}H}$ peak intensity and weakening the O_L peak. The OH from the dissociated water will adsorb on the BFO surface (O_{OH}), however the O 1s binding energy of O_{OH} peak (see simulated XPS spectrum) is too close to the O_L peak to distinguish. The O_L peak both decreases in intensity and broadens, particularly towards higher binding energies with the peak position slightly blue-shifted to 529.8 eV. This can be attributed to the higher band energies in the up-poled sample (**Fig. 2d**), which promote electron transfer from BFO to BVO, decreasing electron density and blue-shifting electron energies in the BFO layer.[47]

The surface atoms can bind more strongly with water due to the surface charge of up-poled BFO.[48] The optimized DFT model for up-poled BFO shows a closer distance between H_2O and the up-poled BFO surface compared to the down-poled BFO surface (**Fig. 4c**, **Supplementary Fig. S20**). The stronger interaction between the up-poled BFO surface and water enhances the $O_{W\text{-}C}$ and $O_{W\text{-}P}$ peaks in the XPS spectra.[44]

The negative charge on the down-poled BFO/BVO surface will promote H^+ adsorption in solution, converting surface lattice O to OH (**Fig. 4d**) giving an enhanced $O_{L\text{-}H}$ peak, as also seen for the up-poled sample (**Fig. 4a and 4b**).[44,49] The $O_{L\text{-}H}$ peak and the BFO lattice oxygen peak (O_L) are blue-shifted due to ferroelectric polarization. The effect is stronger for the O_L than the $O_{L\text{-}H}$ peak, resulting in the two peaks becoming closer where they merge in the experimental result.[49] The peak shifts are seen in the simulated XPS spectra of down-poled BFO (**Fig. 4b**). The O_L and $O_{L\text{-}H}$ peaks both shift by ~ 1 eV to higher binding energies compared with up-poled BFO. The weak O_L peak at lower binding energies in the experimental spectrum is attributed to sub-surface oxygen in BFO, possibly with a contribution from oxygen in BVO. In contrast with the up-poled BFO, the down-poled BFO has a greater distance between the H_2O and the down-poled BFO surface (**Supplementary Fig. S18**), indicating a weaker interaction of the negatively charged down-poled surface. Consequently, the interaction between water and the down-poled sample is dominated by physisorption, indicated by the weaker $O_{W\text{-}C}$ peak and stronger $O_{W\text{-}P}$ peak in both the experimental and simulated spectra. The weaker interaction may allow more fluid interactions in the water environment and more facile product desorption, contributing to the decreased R_f value for down-poled BFO/BVO in this work (**Supplementary Table S2**). In contrast, the up-poled surface binds water very strongly.

Overall, we demonstrate a carefully designed photoanode with high Faradaic efficiency for the OER by integrating ferroelectric BFO and photoactive BVO for PEC water oxidation. The study reveals co-existent competing effects between band shifting, band energy gradient modulation and BFO/water interaction changes for different polarization states. Strikingly, enhancements in PEC performance occur for both polarization directions which, to-date, have not been reported for any ferroelectric-based photoanodes. The down-poled BFO/BVO delivers a 136% enhancement in photocurrent density, being one of the highest reported photocurrent improvements from ferroelectric polarization switching. The findings reveal a shift of BFO band energies to lower band energy levels, invoking intensified band bending at the SEI, and band gradient modulation in down-poled BFO/BVO as the main driver of enhancement. In contrast, band shifting of BFO with up-poled BFO surface drives a 70% enhancement in photocurrent density at 1.23 V_{RHE}. The current study advances the domain of ferroelectric-based photoelectrodes with tunable charge dynamics, offering an additional lever that can achieve the performance limits of traditional static semiconductors for photoelectrochemical applications and beyond.

Author Contributions

Michael Gunawan: Conceptualization, methodology, investigation, formal analysis, writing – original draft preparation. **Owen Bowdler:** Formal analysis, methodology, validation, writing – original draft preparation. **Shujie Zhou:** Methodology, formal analysis, writing – reviewing & editing. **Xueqing Fang:** Formal analysis, validation. **Qi Zhang:** Formal analysis, validation, writing – reviewing & editing. **Yasuhiro Sakamoto:** Formal analysis, investigation. **Kaiwen Sun:** Formal analysis. **Denny Gunawan:** Formal analysis, validation. **Shery L.Y. Chang:** Methodology, resources. **Rose Amal:** Supervision, conceptualization, resources, funding acquisition, writing – reviewing & editing. **Nagarajan Valanoor:** Conceptualization, supervision, resources, funding acquisition, writing – reviewing & editing. **Judy Hart:** Supervision, conceptualization, resources, funding acquisition, writing – reviewing & editing. **Jason Scott:** Supervision, conceptualization, resources, funding acquisition, writing – reviewing & editing. **Cui Ying Toe:** Supervision, conceptualization, methodology, funding acquisition, writing – reviewing & editing.

1 Experimental section

1.1 Sample preparation

The BVO and BFO thin films were prepared using chemical solutions deposition (CSD). To make BVO precursors, 0.004 mol of citric acid was dissolved in 6 mL of 23.3%-v nitric acid (HNO_3). Then 2 mmol of bismuth nitrate pentahydrate ($Bi(NO_3)_3.5H_2O$) and ammonium metavanadate (NH_4VO_3) were added into the solution under vigorous mixing. After the metal precursors dissolved completely, 0.24g of poly(vinyl alcohol) (average M_w 146000-186000, 99% hydrolyzed) and 1.5mL of acetic acid (CH_3COOH) were added to the solution. A BVO photoanode was prepared by spin-coating BVO precursors on cleaned FTO at 3000 rpm for 30 s and the film was dried at 100°C for 5 minutes. The deposition and drying processes were repeated 5 times and the films then annealed in muffle furnace at 500°C for 1 h with a ramping rate of 5°C/min.

BFO precursors were prepared by dissolving 1.68 g of citric acid ($C_6H_8O_7$) into 4 g of ethylene glycol at 90°C. Then, 0.85 g of bismuth nitrate pentahydrate and 0.8 g of iron nitrate nonahydrate ($Fe(NO_3)_3.9H_2O$) were added under constant stirring. The as-synthesized precursors were spin coated onto a BVO thin film (FTO) at rate of 4000 rpm for 60 s. Subsequently, the film underwent a series of heat treatments that consisted of drying (250°C, 5 minutes), and pyrolysis (450°C, 1 hr).

1.2 Sample characterization

Crystalline structure of the samples was investigated by X-ray diffraction (XRD) (PANalytical) with Co Kα radiation at a working potential of 45 kV and a current of 40 mA. Commercial scanning probe microscopy (SPM) (Cypher, Asylum Research, US) was used for kelvin probe force microscopy (KPFM), atomic force microscopy (AFM) and piezoelectric force microscopy (PFM) measurements. UV-VIS Spectroscopy (Shimadzu UV-3600 UV-vis-NIR spectrophotometer) was conducted over 350 nm to 800 nm wavelength with Kubelka-Munk transformation to understand the optical band gap of respective samples. The surface chemical states and energy band structure were analyzed using X-ray photoelectron spectroscopy (XPS) and ultraviolet photoemission spectroscopy (UPS) (Thermo ESCALAB 250Xi) with a mono-chromated Al Kα radiation source (1486.68 eV) and He I excitation light (21.22 eV). All the binding energy values in the XPS spectra were calibrated using C 1s peak at 284.8 eV. The cross-sectional lamellas were prepared using a focused ion beam (FIB) (ThermoFisher Helios G4 PFIB UXe DualBeam) equipped with an Xe plasma FIB ion column and monochromator scanning electron column. STEM imaging was performed by a JEOL JEM-ARM300F2 (GRAND ARM2), double aberration-corrected S/TEM equipped with a cold field emission gun operated at 300 kV. The HAADF images were acquired using the collection semiangles of 90-370 mrad. EDS and EELS elemental analyses were performed on platinum coated sample by JEOL EDS with 158 mm^2 dual SDD and Gatan GIF Continuum with K3 direct electron detector, respectively. Time-resolved photoluminescence (TRPL) characterization was carried out using time-correlated single photon counting (TCSPC) (MicroTime 200, PicoQuant) with an excitation wavelength of 470 nm.

Fe K-edge X-ray absorption spectra (XAS) were recorded on the MEX1 beamline at the Australian Synchrotron, part of ANSTO. The beam energy was 3.0 GeV with a beam current of 200 mA. Data were collected in fluorescence mode. Energies were calibrated against the first inflection point of the Fe foil. XAS data were analyzed using a combination of Sakura for data conversion, Pyspline for background subtractions, and Artemis for extended X-ray absorption fine structure (EXAFS) fitting.

1.3 Electrochemical poling

Ferroelectric poling pretreatment was conducted in an electrochemical cell with BFO/BVO photoanode as the working electrode and Pt plate as the counter electrode. Due to the large electrochemical windows, propylene carbonate solution containing 0.1 M $LiClO_4$ was chosen as the electrolyte for poling pretreatments. The poling bias was controlled in the range between +8 and −8 V; the poling time was 10 s.

1.4 PEC Measurement for Water Splitting

The photoelectrochemical test results such as linear sweep voltammetry (LSV), electrochemical impedance spectroscopy (EIS) Nyquist plot, and chopped chronoamperometry were obtained with a potentiostat (PGSTAT302 N, Autolab) in a one compartment cell with quartz window via a standard three-electrode configuration where platinum (Pt) sheet and saturated Ag/AgCl electrode are used as the counter electrode and reference electrode, respectively. 0.1 M of phosphate buffer solutions (pH = 7) was used as the electrolyte. The photoanode was encapsulated using epoxy with the exposed area fixed to 1 cm^2. To measure the charge separation and injection efficiencies, 0.1 M Na_2SO_3 as a hole scavenger was added to the phosphate buffer solution. A Newport solar simulator was used as the light source, which was calibrated to AM 1.5G (100 mW/cm^2). The yield of oxygen gas was quantified by manual injection into a gas chromatograph (Shimadzu GC-8A) equipped with a TCD detector and Ar as carrier gas.

The potentials were measured versus the Ag/AgCl reference electrode, which can be converted into the reversible hydrogen electrode (RHE) scale by the Nernst equation (Eq. S1):

$$E_{RHE} = E_{Ag/AgCl} + E^0_{Ag/AgCl} + 0.059pH \qquad \text{(Eq. S1)}$$

Where E_{RHE} refers to the converted potential vs. RHE and $E_{Ag/AgCl}$ is the external potential measured against the Ag/AgCl reference electrode. $E^0_{Ag/AgCl}$ represents the standard potential of Ag/AgCl, which is equal to 0.197 V at 25 ºC.

Faradaic efficiency was calculated by dividing the amount of the experimentally generated gas by the theoretical amount of gas which is calculated by the charge passed through the electrode:

Faradaic efficiency (FE)= $V_{experiment}$ / $V_{theoretical}$ = $V_{experiment}$ / $[(1/4)*(Q/F)*V_m]$ where Q is the sum of the charge passed through the photoanode, F is the Faraday constant (96485 C mol^{-2}) and V_m is the molar volume of gas.

1.5 Computational Methods

DFT calculations were done with the CRYSTAL23 code.[50] The B3LYP functional was used, [51-54] with 15% Hartree-Fock exchange energy mixed with the DFT energy, which was found to give densities and band gaps in good agreement with experimental values.[22] D3 dispersion corrections [55-57] and spin polarization were included in all calculations. The basis sets for all elements were of the pob-TZVP-Rev2 type.[58]

After optimization of the bulk bismuth ferrite structure (R3c space group), slabs with a thickness of 3 stoichiometric layers (~10 – 12 Å) were cut exposing the (110) surface. A 2 × 2 supercell in the surface plane was used for all slab calculations with a k-point grid of 3×3×1 (5 k-points in total). To obtain a model of the up-poled structure, the bulk was oriented along the pseudocubic perspective and a region consisting of 3 paired FeO_2 and BiO layers was cut as shown in **Fig. S20**. For the up-poled BFO, the slab consisted of 120 atoms. The stoichiometry of the top layer of the as-cut slab was FeO_2 and the bottom layer was BiO. For the model of down-poled BFO, it was found that the addition of 4 oxygen atoms to the bottom layer gave an energy-minimizing stoichiometry of Bi_2O_3; addition of these oxygens was necessary to achieve convergence in the calculations, resulting in a non-stoichiometric slab of 124 atoms. This was obtained by cutting from the same pseudocubic perspective, but shifted such that the surface FeO_2 and BiO layers were not paired and including additional oxygen on the initial Bi_2O_4

surface, which was then reduced to Bi_2O_3 manually. In the down-poled BVO/BFO sample in the experimental work, the Bi^{3+} ions in the BFO layer at the BVO interface of the are expected to be displaced towards the underlying BVO layer and interact with the oxygen therein, so we believe this addition of stabilizing oxygen on the bottom surface of BFO in the DFT model to be a reasonable representation of the experimental sample. Thus, the down-poled slab model consisted of a total of 124 atoms.

Note that the slab models used in the DFT calculations represent only the BFO component of the BFO/BVO heterostructures and are intended to provide an understanding of the effect of polarization on the electronic and surface structure of BFO. Models were constructed to represent the up-poled and down-poled states only, since the unpoled BFO/BVO has a mixed arrangement of ferroelectric domain orientations, making it difficult to model; it can be considered an intermediate between the up-poled and down-poled models.

A monolayer of water molecules was adsorbed on both the up- and down-poled BFO Fe-terminated surfaces to represent the interaction between polarized BFO and the aqueous electrolyte environment. For the model of up-poled BFO, eight H_2O molecules were added above the surface Fe atoms. For down-poled, H atoms were first added to the eight exposed O atoms on the top surface to form terminating surface hydroxide groups in line with previous studies,[48,59] followed by a second optimization step where eight H_2O molecules were added above the eight Fe atoms exposed at the top surface. The calculated VB and CB energies of -5.7 eV and -3.2 eV, respectively for the (protonated) down-poled state, are in good agreement with our experimental observations (-5.7 eV and -3.1 eV, **Fig. S9 and Fig. S17**).

Acknowledgements

The authors acknowledge the facilities and the scientific and technical assistance of Microscopy Australia at the Electron Microscope Unit (EMU) and other characterization facilities within the Mark Wainwright Analytical Centre (MWAC) at UNSW Sydney. The computational resources necessary for this research were made available by the Australian Government through the National Computational

Infrastructure (NCI) under the National Computational Merit Allocation Scheme. The XAS analysis was undertaken in part using the MEX-1 beamline at the Australian Synchrotron, part of ANSTO (AS241/MEX1/21367). The authors thank Dr. Rosalie Hocking and Dr. Emily Finch for their support and assistance with the XAS measurements. The work was supported by the Australian Research Council (ARC) through Discovery Project (DP210102694), Training Centre for the Global Hydrogen Economy (IC200100023), and Centre of Excellence in Future Low-Energy Electronics Technologies (CE170100039). Q.Z. acknowledges the support of a Women in FLEET Fellowship.

Reference

1 Chu, S., Cui, Y. & Liu, N. The path towards sustainable energy. *Nat. Mater.* **16**, 16-22 (2017).
2 Tan, H. L., Amal, R. & Ng, Y. H. Alternative strategies in improving the photocatalytic and photoelectrochemical activities of visible light-driven $BiVO_4$: a review. *J. Mater. Chem. A* **5**, 16498 (2017).
3 Han, C. *et al.* Nanostructured hybrid catalysts empower the artificial leaf for solar-driven ammonia production from nitrate. *Energy Environ. Sci.* **Advance Article** (2024).
4 Sivula, K. & Krol, R. v. d. Semiconducting materials for photoelectrochemical energy conversion. *Nat. Rev. Mater.* **1**, 15010 (2016).
5 Landman, A. *et al.* Photoelectrochemical water splitting in separate oxygen and hydrogen cells. *Nat. Mater.* **16**, pages646–651 (2017).
6 Toe, C. Y. *et al.* Recent advances and the design criteria of metal sulfide photocathodes and photoanodes for photoelectrocatalysis. *J. Mater. Chem. A* **9**, 20277-20319 (2021).
7 Cui, Y., Briscoe, J. & Dunn, S. Effect of ferroelectricity on solar-light-driven photocatalytic activity of $BaTiO_3$—Influence on the carrier separation and stern layer formation. *Chem. Mater.* **25**, 4215-4223 (2013).
8 Paillard, C. *et al.* Photovoltaics with ferroelectrics: Current status and beyond. *Adv. Mater.* **28**, 5153-5168 (2016).
9 Grinberg, I. *et al.* Perovskite oxides for visible-light-absorbing ferroelectric and photovoltaic materials. *Nature* **503**, 509–512 (2013).
10 Abbasi, P. *et al.* Ferroelectric modulation of surface electronic states in $BaTiO_3$ for enhanced hydrogen evolution activity. *Nano Lett.* **22**, 4276–4284 (2022).
11 Kakekhani, A. & Ismail-Beigi, S. Ferroelectric-based catalysis: Switchable surface chemistry. *ACS Catal.* **5**, 4537-4545 (2015).
12 Wang, Z. *et al.* Manipulation of charge transfer and transport in plasmonic-ferroelectric hybrids for photoelectrochemical applications. *Nat. Commun.* **7**, 10348 (2016).
13 Augurio, A. *et al.* Controlled Porosity in Ferroelectric $BaTiO_3$ Photoanodes. *ACS Appl. Mater. Interfaces* **14**, 13147–13157 (2022).
14 Magnan, H. *et al.* Tuning the charge carriers migration in epitaxial $BaTiO_3$ thin-film photoanodes. *J. Phys. Chem. C.* **124**, 10315-10323 (2020).
15 Singh, S., Sangle, A. L., Wu, T., Khare, N. & MacManus-Driscoll, J. L. Growth of doped $SrTiO_3$ ferroelectric nanoporous thin films and tuning of photoelectrochemical properties with switchable ferroelectric polarization. *ACS Appl. Mater. Interfaces* **11**, 45683-45691 (2019).

16 Assavachin, S. & Osterloh, F. E. Ferroelectric polarization in $BaTiO_3$ nanocrystals controls photoelectrochemical water oxidation and photocatalytic hydrogen evolution. *J. Am. Chem. Soc.* **145**, 18825–18833 (2023).

17 Xia, C., Wang, H., Kim, J. K. & Wang, J. Rational design of metal oxide-based heterostructure for efficient photocatalytic and photoelectrochemical systems. *Adv. Funct. Mater.* **31**, 2008247 (2021).

18 Wang, J. *et al.* Epitaxial $BiFeO_3$ multiferroic thin film heterostructures. *Science* **299**, 1719-1722 (2003).

19 Yang, S. Y. *et al.* Above-bandgap voltages from ferroelectric photovoltaic devices. *Nat. Nanotechnonl.* **5**, 143–147 (2010).

20 Choi, T., Lee, S., Choi, Y. J., Kiryukhin, V. & Cheong, S.-W. Switchable ferroelectric diode and photovoltaic effect in $BiFeO_3$. *Science* **324**, 63-66 (2009).

21 Yi, H. T., Choi, T., Choi, S. G., Oh, Y. S. & Cheong, S.-W. Mechanism of the switchable photovoltaic effect in ferroelectric $BiFeO_3$. *Advanced Materials* **23**, 3403-3407 (2011).

22 Li, X. *et al.* Polarization alignment in polycrystalline $BiFeO_3$ photoelectrodes for tunable band bending. *ACS Nano* **17**, 22944−22951 (2023).

23 Ji, W., Yao, K., Lim, Y.-F., Liang, Y. C. & Suwardi, A. Epitaxial ferroelectric BiFeO3 thin films for unassisted photocatalytic water splitting. *Appl. Phys. Lett.* **103**, 062901 (2013).

24 Cao, D. *et al.* Switchable charge-transfer in the photoelectrochemical energy-conversion process of ferroelectric $BiFeO_3$ photoelectrodes. *Angew. Chem., Int. Ed.* **53**, 11027-11031 (2014).

25 Xie, J. *et al.* Bi-functional ferroelectric $BiFeO_3$ passivated $BiVO_4$ photoanode for efficient and stable solar water oxidation. *Nano Energy* **31**, 28-36 (2017).

26 Kim, T. W. & Choi, K.-S. Nanoporous $BiVO_4$ photoanodes with dual-layer oxygen evolution catalysts for solar water splitting. *Science* **343**, 990-994 (2014). https://doi.org/doi:10.1126/science.1246913

27 Yang, M.-M. *et al.* Auxetic piezoelectric effect in heterostructures. *Nat. Mater.* **23**, 95-100 (2024).

28 Yang, Z., Zhao, L., Zhang, S. & Zhao, X. Ferroelectric-enhanced $BiVO_4$ -$BiFeO_3$ photoelectrocatalysis for efficient, stable and large-current-density oxygen evolution. *Appl. Mater.* **26**, 101374 (2022).

29 Soltani, T., Tayyebi, A. & Lee, B.-K. $BiFeO_3$/$BiVO_4$ p−n heterojunction for efficient and stable photocatalytic and photoelectrochemical water splitting under visible-light irradiation. *Catalysis Today* **340**, 188-196 (2020). https://doi.org/https://doi.org/10.1016/j.cattod.2018.09.030

30 Afroz, K., Moniruddin, M., Bakranov, N., Kudaibergenov, S. & Nuraje, N. A heterojunction strategy to improve the visible light sensitive water splitting performance of photocatalytic materials. *J. Mater. Chem. A* **6**, 21696-21718 (2018).

31 Huang, J. *et al.* Synergistically enhanced charge separation in $BiFeO_3$/Sn:TiO_2 nanorod photoanode via bulk and surface dual modifications *Nano Energy* **59**, 33-40 (2019).

32 Sima, M. *et al.* Effect of ferroelectric poling on the photoelectrochemical activity of hematite-$BaTiO_3$ nanowire arrays. *Int. J. Hydrogen Energy* **46**, 36232-36244 (2021).

33 Rioult, M. *et al.* Tailoring the photocurrent in $BaTiO_3$/Nb:$SrTiO_3$ photoanodes by controlled ferroelectric polarization. *Appl. Phys. Lett.* **107**, 103901 (2015).

34 Liu, Z. *et al.* Piezoelectric-effect-enhanced full-spectrum photoelectrocatalysis in p–n heterojunction. *Adv. Funct. Mater.* **29**, 1807279 (2019).

35 Wu, F. *et al.* Simultaneous enhancement of charge separation and hole transportation in a TiO_2–$SrTiO_3$ core–shell nanowire photoelectrochemical system. *Adv. Mater.* **29**, 1701432 (2017).

36 Singh, S. & Khare, N. Flexible PVDF/Cu/PVDF-$NaNbO_3$ photoanode with ferroelectric properties: An efficient tuning of photoelectrochemical water splitting with electric field polarization and piezophototronic effect. *Nano Energy* **42**, 173-180 (2017).

37 He, X. *et al.* Novel Fe_2O_3/PZT nanorods for ferroelectric polarization-enhanced photoelectrochemical water splitting. *Energy Fuels* **34**, 16927-16935 (2020).

38 Lewis, N. S. Chemical control of charge transfer and recombination at semiconductor photoelectrode surfaces. *Inorg. Chem.* **44**, 6900–6911 (2005).

39 Mundy, J. A. *et al.* Functional electronic inversion layers at ferroelectric domain walls. *Nat. Mater.* **16**, 622–627 (2017).
40 Yang, W. *et al.* Ferroelectric polarization-enhanced photoelectrochemical water splitting in TiO_2–$BaTiO_3$ core–shell nanowire photoanodes. *Nano Lett.* **15**, 7574-7580 (2015).
41 Abnavi, H., Maram, D. K. & Abnavi, A. Performance analysis of several electron/hole transport layers in thin film $MAPbI_3$-based perovskite solar cells: A simulation study. *Opt. Mater.* **118**, 111258 (2021).
42 Bhatnagar, A., Chaudhuri, A. R., Kim, Y. H., Hesse, D. & Alexe, M. Role of domain walls in the abnormal photovoltaic effect in $BiFeO_3$. *Nat. Commun.* **4**, 2835 (2013).
43 Wang, S., Chen, P., Yun, J.-H., Hu, Y. & Wang, L. An electrochemically treated $BiVO_4$ photoanode for efficient photoelectrochemical water splitting. *Angew. Chem. Int. Ed.* **56**, 8500-8504 (2017).
44 Chen, X., Liu, C., Hua, Z. & Ma, N. Ferroelectric polarization and oxygen vacancy synergistically induced an ultrasensitive and fast humidity sensor for multifunctional applications. *ACS Appl. Mater. Interfaces* **14**, 49965–49974 (2022).
45 Rojac, T. *et al.* Domain-wall conduction in ferroelectric $BiFeO_3$ controlled by accumulation of charged defects. *Nat. Mater.* **16**, 322–327 (2017).
46 Bencan, A. *et al.* Domain-wall pinning and defect ordering in $BiFeO_3$ probed on the atomic and nanoscale. *Nat. Commun.* **11**, 1762 (2020).
47 Jing, Q. *et al.* Boosting piezo-photocatalytic activity of $BiVO_4$/$BiFeO_3$ heterojunctions through built-in polarization field tailoring carrier transfer performances. *Chem. Eng. J.* **464**, 142617 (2023).
48 Efe, I., Spaldin, N. A. & Gattinoni, C. On the happiness of ferroelectric surfacesand its role in water dissociation: The example of bismuth ferrite. *J. Chem. Phys.* **154**, 024702 (2021).
49 Li, X. *et al.* Engineering polarization in the ferroelectric electrocatalysts to boost water electrolysis. *Adv. Funct. Mater.* **33**, 2210194 (2023).
50 Erba, A. *et al.* CRYSTAL23: A program for computational solid state physics and chemistry. *J. Chem. Theory Comput.* **19**, 6891–6932 (2023).
51 Becke, D. Density - functional thermochemistry. III. The role of exact exchange. *J. Chem. Phys.* **98**, 5648–5652 (1993).
52 Lee, W. Yang & Parr, R. G. Development of the Colle-Salvetti correlation-energy formula into a functional of the electron density. *Phys. Rev. B.* **37**, 785 (1988).
53 Vosko, H., Wilk, L. & M. Nusair. Accurate spin-dependent electron liquid correlation energies for local spin density calculations: a critical analysis. *Can. J. Phys.* **58**, 1200–1211 (1980).
54 Stephens, J., Devlin, F. J., Chabalowski, C. F. & Frisch, M. J. Ab initio calculation of vibrational absorption and circular dichroism spectra using density functional force fields. *J. Phys. Chem.* **98**, 11623–11627 (1994).
55 Grimme, S., Antony, J., Ehrlich, S. & Krieg, H. A consistent and accurate ab initio parametrization of density functional dispersion correction (DFT-D) for the 94 elements H-Pu *J. Chem. Phys.* **132**, 154104 (2010).
56 Grimme, S., Ehrlich, S. & Goerigk, L. Effect of the damping function in dispersion corrected density functional theory. *J. Comput. Chem.* **32**, 1456-1465 (2011).
57 Grimme, S., Hansen, A., Brandenburg, J. G. & Bannwarth, C. Dispersion-corrected mean-field electronic structure methods. *Chem. Rev.* **116**, 5105–5154 (2016).
58 Laun, J. & Bredow, T. BSSE-corrected consistent Gaussian basis sets of triple-zeta valence with polarization quality of the sixth period for solid-state calculations. *J. Comput. Chem.* **42**, 1064-1072 (2021).
59 Tian, Y. *et al.* Water printing of ferroelectric polarization. *Nat. Commun.* **9**, 3809 (2018).

TOC

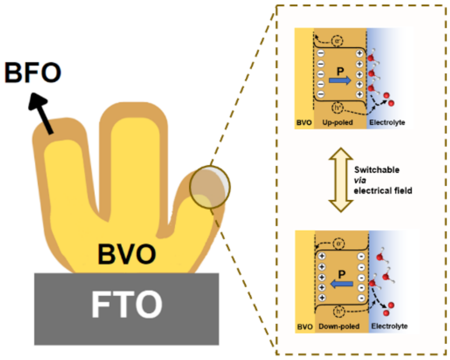

The spontaneous and reversible polarization of a ferroelectric photoanode influences its electronic and surface structure, thereby regulating its photoelectrochemical performance. In this study, the individual effects of polarization switching, band energies shifts, band energy gradients modulation, and changes in the water/BFO interaction of a BFO/BVO photoanode was systematically unraveled.